The IRM Quarterly
Winter 2021-2022, Vol. 31 No. 4
ISSN: 2152-1972

Inside...

A case for adopting the magnetic core alternating field demagnetizer

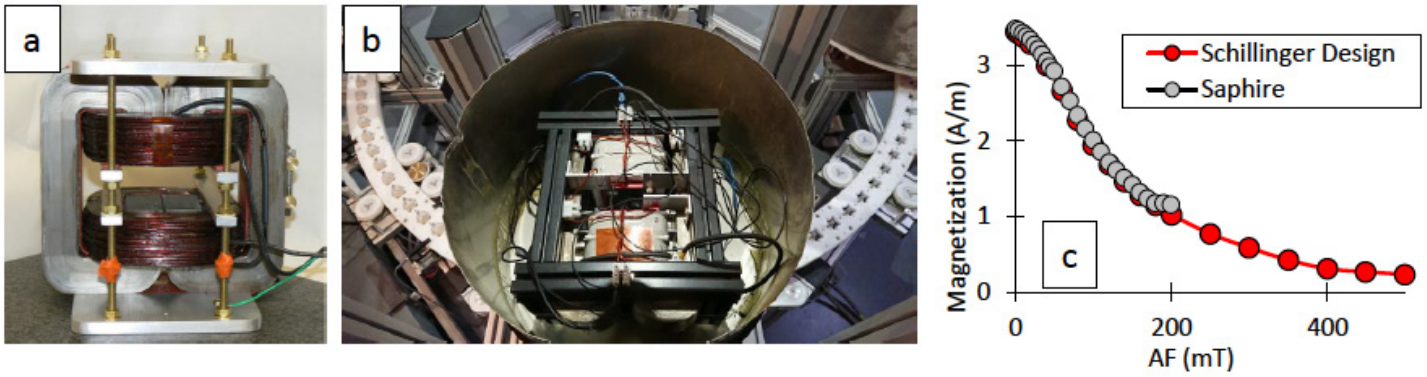

Figure 1. Schillinger Metglas magnetic-core design for (a) the alternating field demagnetizers at UCSC and (b) that implemented on the SushiBar at LMU-Munich. (c) Comparison of NRM demagnetization of two sister samples collected from the strongly welded and rheomorphic basal vitrophyre of a Snake River (SR-type) Ignimbrite (Data from Schillinger et al. 2016).

David Finn*[1,2], Michael Wack[3], Leon Kaub[3], Stuart Gilder[3], Rob Coe[2], Walter Schillinger[2], Michael Branney[1]

*dfinn@ucsc.edu

[1]School of Geography, Geology and the Environment, University of Leicester, UK

[2]University of California Santa Cruz, Santa Cruz, USA

[3]Ludwig Maximilians University, Department of Earth and Environmental Sciences, Munich, Germany

1. Introduction

Paleomagnetic studies improve our understanding of a myriad of geologic processes. Laboratory methods to acquire paleomagnetic information are well established and often used without questioning their effectiveness. These decades-old methods (e.g., three-axis static alternating field [AF] demagnetization) were adopted according to the technical capabilities of the time. However, since the 1960-1980s, the capabilities of instrumentation have substantially advanced, which provides an opportunity for implementation of more useful laboratory methods.

A notable improvement to instrumentation is the Schillinger AF demagnetizer (Schillinger et. al. 2016), which employs a Metglas core with coils wound around it (Figure 1a & b). This works like an electromagnet except that Metglas has almost zero remanence (unlike the steel used in electromagnets), so it can still produce a pure AF signal in the air gap to demagnetize rocks without imparting anhysteretic remanence (ARM). The advantage over air-core based AF systems is that much lower currents are required to produce a given field, so the Schillinger design can achieve a peak AF field at least two to three times larger than conventional systems without overheating (Figure 1c). Because the field lines are largely confined within the gap, two nested mu-metal shields are sufficient to prohibit stray AC fields from leaking into the local environment and, within a shielded room, to reduce DC fields to a few tens of nanoteslas. Another feature of the design is that it applies the AF orthogonal, rather than parallel, to the demagnetizer's sample access (i.e., the borehole). This enables substantial improvements to some common laboratory measurements by allowing for any arbitrary AF or ARM orientation to easily be obtained. We will elaborate on advantages to various applications in the article that follows the main body of this IRM issue.

cont'd. on pg. 9...

Visiting Fellow Reports

Applied methods of magnetic analysis to determine the mechanism of bubble nucleation in Plinian eruptions of aphyric rhyolite

Kelly McCartney
University of Hawaii at Manoa
kmccartn@hawaii.edu

Julia Hammer
University of Hawaii at Manoa

Stephanie Brachfeld
Montclair State University

Introduction

For gas to exsolve from a silicic melt, significant supersaturation pressures are required. This supersaturation pressure is minimized via the presence of a nucleation substrate (heterogeneous nucleation; <25 MPa) and maximized if no nucleation substrate is present (homogeneous nucleation; >100 MPa; Shea, 2017; Figure 1). Conventionally, erupted rhyolite pumice is assessed for the presence of a crystal phase that is equal to or greater than the bubble number density (BND) found in the pumice. If no such phase can be identified, the eruption is assumed to result from homogenous bubble nucleation. However, many crystal-poor eruptions have come from magma chambers that are too shallow to generate the required pressures. This inconsistency necessitates a reevaluation of how the process of bubble nucleation occurs in these high silica systems.

The methods conventionally used to determine the presence of a potential nucleation substrate (petrographic microscope, electron microscopy, X-ray tomography) suffer from limited spatial resolutions, severely limiting the ability to detect sub-µm crystals (Sahagian and Proussevitch, 1992; Shea et al., 2010; Shea, 2017). As such, sub-µm crystals go undetected, and their number densities are unknown. Titanomagnetite is a relatively common and early forming mineral in these high silica systems. Magnetic analyses can therefore be applied to determine if titanomagnetite is present in these systems on the nanometer scale, and estimate the titanomagnetite number densities (TND) it which they occur. This allows the investigation into nanometer scale titanomagnetite as a previously overlooked nucleation mechanism in otherwise crystal poor rhyolite.

Magnetic methodologies (like those of Worm and Jackson, 1999) can be used to investigate the presence, abundance, and mineralogy of magnetic minerals present in rhyolite pumice and obsidian from the 1100 AD Glass Mountain eruption (California, USA, subplinian eruption, ~3% phenocrysts, 73% SiO2, 1-3 km depth; Grove et al., 1997). This eruption generated ~1km3 (dense rock equivalent) of crystal poor obsidian flows and pumice fall deposits used for this project. If titanomagnetite crystals are present on the nanometer scale, and in number densities greater than bubble number densities, then titanomagnetite may have been a substrate for heterogenous nucleation in these systems (Shea et al., 2016, 2017; McCartney et al., 2020, 2021).

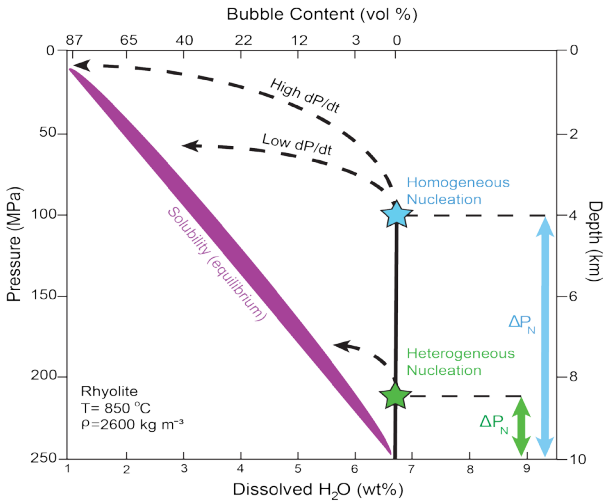

Figure 1: Nucleation style determines the efficiency of degassing in rhyolite melt. The purple region designates the path of solubility of a rhyolite system at 850 °C from 250 MPa to 0 MPa. The path followed by the system is dependent on the style of nucleation, with heterogeneous nucleation (green) returning the system to equilibrium sooner than homogeneous nucleation (blue). Modified after: Shea, 2017; Mangan and Sisson 2000.

Experiments

Preliminary rock magnetic analyses were conducted at Montclair State University to confirm the presence of titanomagnetite in both the pumice and obsidian using mass normalized susceptibility (χ, subsequently converted to volume-normalized k), frequency dependence of susceptibility ($\%\chi_{FD}$), anhysteretic remanent magnetization (ARM), Curie temperature analysis, and hysteresis behavior (McCartney et al., 2020, 2021). We approximated grain size by comparing the grain size-sensitive ratio χ/χ_{ARM} for the pumice and obsidian to published χ/χ_{ARM} values of natural and synthetic (titano)magnetite's with known grain sizes (Maher, 1988; Till et al., 2011). Both pumice and obsidian are consistent with χ/χ_{ARM} values measured on 10-30 nm magnetite crystals, though larger multidomain crystals cannot be ruled out (Figure 2). Due to the lack of abundant conventionally observable micron scale particles, it is likely that the majority of titanomagnetite particles present are on the nanometer scale.

Work done at the IRM consisted of low temperature

magnetic characterization conducted on a Quantum Design Magnetic Properties Measurement System (MPMS-3) in order to investigate the presence of superparamagnetic particles. We measured hysteresis loops at 5 K and 20 K, and observed the behavior of a saturation isothermal remanent magnetization during warming. In a field cooled-zero field cooled (FC-ZFC) experiment, a saturation isothermal remanent magnetization (M_R (5 K)) was imparted during cooling from 300 K in the presence of a 2.5 T field (FC = field cooled), and again at 5 K in a 2.5 T field after cooling from 300 K in zero applied field (ZFC = zero field cooled), in both cases measuring the remanent magnetization on warming. These measurements may reveal order-disorder transitions related to mineral composition and/or behaviors suggestive of single domain and multidomain grains (e.g., Moskowitz, 1993; Jackson et al., 1998; Moskowitz et al., 1998; Carter-Stiglitz et al., 2006). Our goal was to identify samples with SP characteristics and ultimately apply the methods of Worm and Jackson, 1999, to calculate a grain size distribution. We then measured susceptibility vs. temperature at 3 frequencies to look for signatures of SP particles.

Results

χ/χ_{ARM} values for the pumice and obsidian are consistent with 10-30 nm or 1-10 µm titanomagnetite. Assuming a single particle size with cubic shape allows for the number density of titanomagnetite crystals to be estimated by dividing the total volume of titanomagnetite, estimated from magnetic susceptibility, by the individual crystal volume. If only nm scale crystals are present, then TND is on the order of ~$1*10^{18}$-10^{20} m^{-3} for the pumice and obsidian. If only µm scale crystals are present, then TND is on the order of $1*10^{10}$-10^{14} m^{-3}. Reported average BND for Glass Mountain pumice is $4*10^{14}$ m^{-3}. Thus, TND > BND by several orders of magnitude if the majority of titanomagnetite particles are on the nm scale (Figure 2).

Low temperature hysteresis loops (not shown) on our pilot sample did not show the expected dramatic change from SP at room temperature to SSD at low temperature. We speculate that in the samples we analyzed, the MD particles dominated the low temperature signal.

FC-ZFC curves are similar for both the pumice and obsidian samples. We observed three types of results: (1) samples for which the ZFC curve is stronger than the FC curve, consistent with low temperature observations of multidomain titanomagnetites described by Carter-Stiglitz et al., 2006; (2) samples for which the ZFC and FC curves are nearly the same and which display a titanomagnetite order-disorder transition at ~55-65 K; (3) samples that do not have a prominent order-disorder transition (Figure 3). While the pumice and obsidian samples likely contain nm titanomagnetite, results of type 1 and 2 indicate samples whose low temperature behavior is dominated by µm-sized and larger particles. Samples that exhibit behavior #3, interpreted as thermal unblocking only, are targets for future experiments that seek to confirm the presence of SP particles using low temperature hysteresis and FORC techniques. These samples will be used for particle distribution calculations.

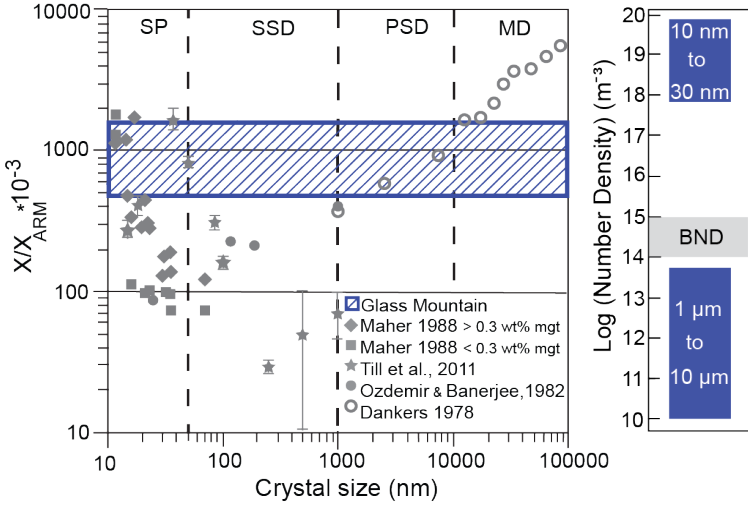

Figure. 2: Left: χ/χARM values for natural and synthetic magnetite of known sizes plotted vs. crystal size form a rough parabola. Vertical lines show grain size transitions between superparamagnetic (SP), stable single domain (SSD), pseudo single domain (PSD), and multidomain (MD) magnetite. The range of Glass Mountain χ/χARM values are encompassed by the blue crosshatched region, which intersect the parabola and provide two possible grain size solutions (nm and µm scale). Right: Calculated TNDs for the nm and µm scale grain size solutions are represented by the vertical bars, and represent the range of ND possible for the range of crystal size diameters. Calculated values fall above and below the average BND, with the true TND likely falling nearer the nm estimate, as the majority of particles are likely on the nm scale.

The culmination of this evidence indicates that titanomagnetite is present in large number densities at the nm scale and outnumbers bubble number densities by upwards of 3-5 orders of magnitude within both the pumice and obsidian samples. This indicates that bubble nucleation in crystal poor silicic eruptions may be generated via heterogeneous nucleation on abundant nm scale titanomagnetite crystals.

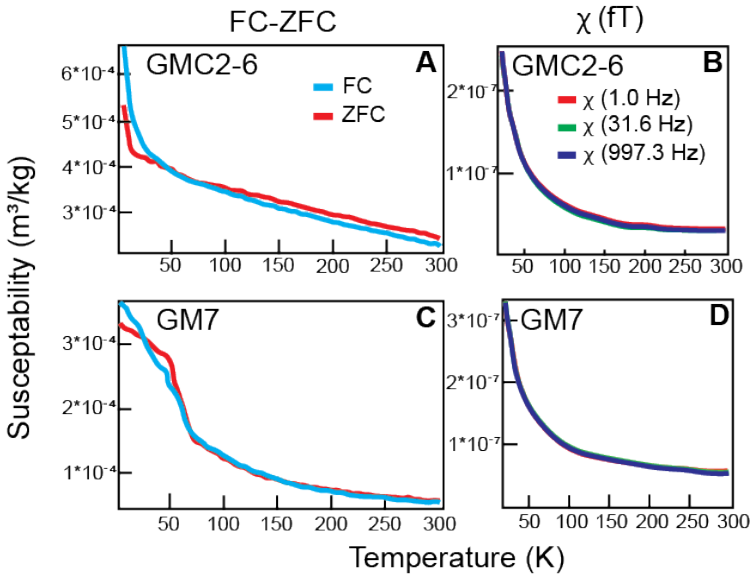

Figure 3: FC-ZFC curves (A and C) of the pumice (GMC2-6) and obsidian (GM7) lack the magnetite Verwey transition. GM7's ZFC curve shows an order-disorder transition at ~55-65K which is consistent with titanomagnetite. χ (fT) (B and D) curves are dominated by paramagnetic behavior.

Acknowledgments

We thank Dario Bilardello, Maxwell Brown, Peat Sølheid, Joshua Feinberg and Bruce Moskowitz for their assistance, guidance, and helpful discussions during this visit. We also thank Thomas Shea and Thomas Giachetti for there contributions to this work.

References

Carter-Stiglitz, B., B. Moskowitz, P. Solheid, T. S. Berquo´, M. Jackson, and A. Kosterov (2006), Low-temperature magnetic behavior of multidomain titanomagnetites: TM0, TM16, and TM35, J. Geophys. Res., 111, B12S05.

Dankers P.H.M., 1978. Magnetic Properties of Dispersed Natural Iron-Oxides of Known Grain-Size. Ph.D. thesis, Univ. of Utrecht, The Netherlands

Grove, T.L., Donnelly-Nolan, J.M., Housh, T., 1997. Magmatic processes that generated the rhyolite of Glass Mountain, Medicine Lake volcano, N. Sahagian, D., Proussevitch, A., 1992. Bubbles in volcanic systems. Scientific Correspondence, v. 359, p. 485.

Mangan, M., Sisson, T., 2000. Delayed, disequilibrium degassing in rhyolite magma: decompression experiments and implications for explosive volcanism. Earth and Planetary Science Letters, v. 183, pg. 441–455.

Maher, B.A., 1988. Magnetic properties of some synthetic submicron magnetite's. Geophysical Journal International, v. 94, pg. 83–96.

McCartney, K.N., Hammer, J.E., Shea, T., Giachetti, T., Brachfeld, S., 2020. Investigating titanomagnetite abundance in rhyolite pumice, Goldschmidt Virtual 2020.

McCartney, K., Hammer, J., Shea, T., Brachfeld, S., Giachetti, T., 2021. Addressing the Mechanism of Bubble Nucleation in Aphyric Rhyolite Using Rock-Magnetism, Fall 2021 American Geophysical Union.

Moskowitz, B.M., Frankel, R.G., Bazylinski, D.A. 1993. Rock magnetic criteria for the detection of biogenic magnetite, Earth Planet. Sci. Lett. 120. 283-300.

Moskowitz, B.M, Jackson, M.J., Kissel, C. 1998. Low-temperature magnetic behavior of titanomagnetites, Earth Planet. Sci. Lett. 157 (1998) 141-149.

Özdemir, Ö., Banerjee, S.K., 1982. A preliminary magnetic study of soil samples from west-central Minnesota. Earth and Planetary Science Letters, v. 59, pg. 393–403.

Till, J.L., Jackson, M.J., Rosenbaum, J.G., Solheid, P., 2011. Magnetic properties in an ash flow tuff with continuous grain size variation: A natural reference for magnetic particle granulometry. Geochemistry, Geophysics, Geosystems, v. 12, pg. 1-10.

Sahagian, D., Proussevitch, A., 1992. Bubbles in volcanic systems. Scientific Correspondence, v. 359, p. 485.

Shea, T., Houghton, B.F., Gurioli, L., Cashman, K.V., Hammer, J.E., Hobden, B.J., 2010. Textural studies of vesicles in volcanic rocks: An integrated methodology. Journal of Volcanology and Geothermal Research v. 190, pg. 271–289.

Shea, T., Hammer, J., Brachfeld, S., 2016. Bubble nucleation in magmas: a dominantly heterogeneous process? Fall 2016 Meeting of the American Geophysical Union, San Francisco, CA.

Shea, T., 2017. Bubble nucleation in magmas: A dominantly heterogeneous process? Journal of Volcanology and Geothermal Research, v. 343, pg. 155–170.

Worm, H.-U., Jackson, M., 1999. The superparamagnetism of Yucca Mountain Tuff. Journal of Geophysical Research, v.

Visiting Fellows

January - July, 2022

Leyla Namazie

University of California, Berkeley

Rock Magnetic Characterization of Volcanic Sediments in the Carboniferous Baird Formation

Miles Harbury

University of Wisconsin -Milwaukee

Determining Genetic Origins of Early Proterozoic Diamictites using Anisotropy of Magnetic Susceptibility (AMS).

Jack Turney

Imperial College London

Magnetic enhancements at past and present oil water contacts in hydrocarbon reservoirs: Wytch Farm oilfield, Wessex Basin, UK

Deepa Dwyer

Oregon State University

Determining source and transport mechanisms using magnetic mineral assemblage during Siku Event 1

Vitor Silvera

Observatorio Nacional (ON MCTI), Rio de Janeiro, Brazil

Joint rock magnetism, AMS and 3D seismic investigation of IODP sites U1461 and U1463: an evaluation of the Plio Pleistocene paleoclimate and paleoceanographic changes recorded at the NW Shelf of Australia

Hassan Aftab Sheikh

University of Cambridge

A nano environmental magnetism approach to biomagnetic air pollution monitoring

Roger Hart

University of Rhode Island

Magnetic Survey of Serpentinized Ultramafics Across Different Tectonic Settings

Romina Achaga

Universidad Nacional del Centro de la Provincia de Buenos Aires

Determination of paleoenvironmental and paleomagnetic variations in the Argentine Pampean Plains using sediments of Cabeza de Buey Lake

Current Articles

A list of current research articles dealing with various topics in the physics and chemistry of magnetism is a regular feature of the IRM Quarterly. Articles published in familiar geology and geophysics journals are included; special emphasis is given to current articles from physics, chemistry, and materials-science journals. Most are taken from ISI Web of Knowledge, after which they are subjected to Procrustean culling for this newsletter. An extensive reference list of articles (primarily about rock magnetism, the physics and chemistry of magnetism, and some paleomagnetism) is continually updated at the IRM. This list, with more than 10,000 references, is available free of charge. Your contributions both to the list and to the Current Articles section of the IRM Quarterly are always welcome.

Archaeomagnetism

de Lumley, H. (2022), Did the first inhabitants of the Caune de l'Arago between 700,000 and 400,000 years BP have domesticated fire? Did they know how to light the fire at will?, Comptes Rendus Geoscience, 354, 41-45, doi:10.5802/crgeos.113.

Deldicque, D., J. P. Pozzi, C. Perrenoud, C. Falgueres, G. Mahieux, A. S. Lartigot-Campin, and J. N. Rouzaud (2021), Search for early traces of fire in the Caune de l'Arago at Tautavel (Eastern Pyrenees, France), combining magnetic susceptibility measurements, microscopic observations, and Raman analysis, Comptes Rendus Geoscience, 353(1), 247-264, doi:10.5802/crgeos.66.

Deldicque, D., J. P. Pozzi, C. Perrenoud, C. Falgueres, G. Mahieux, A. S. Lartigot-Campin, and J. N. Rouzaud (2022), Traces of fire in a 560,000-year-old occupation soil at Caune de l'Arago: response to the article by Professor Henry de Lumley, Comptes Rendus Geoscience, 354, 47-50, doi:10.5802/crgeos.114.

Gallet, Y. (2021), The dawn of archeomagnetic dating, Comptes Rendus Geoscience, 353(1), 285-296, doi:10.5802/crgeos.73.

Kostadinova-Avramova, M., A. Kosterov, N. Jordanova, P. Dimitrov, and M. Kovacheva (2021), Geomagnetic field variations and low success rate of archaeointensity determination experiments for Iron Age sites in Bulgaria, Physics of the Earth and Planetary Interiors, 320, doi:10.1016/j.pepi.2021.106799.

Tema, E., E. Ferrara, L. Zamboni, M. Venturino, M. Reboldi, A. E. Guevara, and L. Casas (2022), Determining the use of ancient ceramic artefacts through combined morphological and magnetic analyses: the case of Villa del Foro, Northern Italy, Archaeological and Anthropological Sciences, 14(1), doi:10.1007/s12520-021-01472-4.

Environmental Magnetism

Abe, H., N. Kawamura, N. Ishikawa, and T. Kogiso (2022), Changes in elements and magnetic properties of Sendai Bay sediments caused by the 2011 Tohoku-oki tsunami, Island Arc, 31(1), doi:10.1111/iar.12437.

Chou, Y. M., X. D. Jiang, L. Lo, L. C. Wang, T. Q. Lee, C. C. Wang, Y. X. Pan, J. J. Zou, F. Humbert, and Z. Q. Liu (2021), Controls on Terrigenous Detritus Deposition and Oceanography Changes in the Central Okhotsk Sea Over the Past 1550 ka, Frontiers in Earth Science, 9, doi:10.3389/feart.2021.683984.

Dash, C., R. Shankar, P. Pati, B. R. Manjunatha, R. A. Shah, and J. Jose (2022), p Changes in the Indian Summer Monsoon during the past 600 years: A high-resolution record from the Anshupa Lake, Upper Mahanadi Delta, Core Monsoon Zone of India, Journal of Asian Earth Sciences, 226, doi:10.1016/j.jseaes.2021.105048.

Dong, K., S. Q. Qiao, B. Wu, X. F. Shi, Y. F. Chen, X. Shan, S. F. Liu, N. Kornkanitnan, and S. Khokiattiwong (2021), Sedimentary History of Trace Metals Over the Past Half-Century in Songkhla Lake, Western Coast of the Gulf of Thailand: Anthropogenic Impacts and Contamination Assessment, Frontiers in Earth Science, 9, doi:10.3389/feart.2021.767899.

Feinberg, J. M., and K. K. Hobart (2021), Attraction in the Dark: The Magnetism of Speleothems, Elements, 17(2), 113-118, doi:10.2138/gselements.17.2.113.

Feng, Z. T., W. L. Zhang, T. Zhang, X. M. Fang, J. B. Zan, M. D. Yan, C. H. Song, T. Li, W. X. Ning, and H. Wang (2021), Early-Middle Eocene Hydroclimate Variations Recorded by Environmental Magnetism in the Linxia Basin, NE Tibetan Plateau, Paleoceanography and Paleoclimatology, 36(11), doi:10.1029/2021pa004338.

Griffing, C. Y., J. J. Clague, R. W. Barendregt, B. Ercolano, H. Corbella, J. Rabassa, and N. J. Roberts (2022), Early and Middle Pleistocene glaciation of the southern Patagonian plain, Journal of South American Earth Sciences, 114, doi:10.1016/j.jsames.2021.103687.

Murthuza, K. M., N. Surumbarkuzhali, C. L. Narasimhan, V. Thirukumaran, A. Chandrasekaran, D. Ganesh, and R. Ravisankar (2022), Magnetic and soil parameters as a potential indicator of soil pollution in the district of Tiruvannamalai, Tamil Nadu, India, Environmental Earth Sciences, 81(3), doi:10.1007/s12665-022-10196-0.

Parth, S., J. Russell, and N. Waldmann (2021), Reconstructing 1200 years of Hydroclimate Variability in the Southern Margins of the Arabian Desert: Insights From a Paleo-Lake in Southern Yemen, Frontiers in Earth Science, 9, doi:10.3389/feart.2021.712443.

Ryang, W. H., A. R. Simms, H. H. Yoon, S. S. Chun, and G. S. Kong (2022), Last interglacial sea-level proxies in the Korean Peninsula, Earth System Science Data, 14(1), 117-142, doi:10.5194/essd-14-117-2022.

Shin, J. Y., K. Hyeong, and W. Kim (2021), A Sediment Magnetic Record in the North Pacific Across the Mid-Pleistocene Transition and its Implication on Asian Dust Evolution, Frontiers in Earth Science, 9, doi:10.3389/feart.2021.789584.

Silveira, V. E. P., et al. (2021), Environmental magnetism evidence for longshore drift distribution of Fe-bearing phases: an example from the Brazilian southeastern coastal region, Journal of Sedimentary Research, 91(11), 1133-1150, doi:10.2110/jsr.2020.089.

Song, Y. G., et al. (2021), Spatio-temporal distribution of Quaternary loess across Central Asia, Palaeogeography Palaeoclimatology Palaeoecology, 567, doi:10.1016/j.palaeo.2021.110279.

Sun, J., et al. (2022), The sedimentary succession of the last 2.25 Myr in the Bohai Strait: Implications for the Quaternary paleoenvironmental evolution of the Bohai Sea, Palaeogeography Palaeoclimatology Palaeoecology, 585, doi:10.1016/j.palaeo.2021.110704.

Tan, M. Q., W. L. Zhang, X. M. Fang, M. D. Yan, J. B. Zan, and T. Zhang (2020), Rock magnetic record of core SG-3 since 1 Ma in the western Qaidam Basin and its paleoclimate implications for the NE Tibetan Plateau, Palaeogeography Palaeoclimatology Palaeoecology, 560, doi:10.1016/j.palaeo.2020.109949.

Vilela, F. T., A. Pedrosa-Soares, M. Babinski, C. Lana, R. I. F. Trindade, and E. Santos (2021), Diamictitic iron forma-

tion (DIF) deposits of the Neoproterozoic Nova Aurora Iron District (Macaubas Group, Southeast Brazil), Journal of South American Earth Sciences, 112, doi:10.1016/j.jsames.2021.103614.

Wang, F., W. G. Zhang, T. Q. Huang, Y. T. Xu, and Z. P. Lai (2022), Particle-size dependent magnetic property variations in the Yangtze delta sediments of late Holocene: Effects of pedogenesis and diagenesis, Catena, 209, doi:10.1016/j.catena.2021.105832.

Warrier, A. K., B. S. Mahesh, J. G. Sebastian, and R. Mohan (2021), How strong was pedogenesis in Schirmacher Oasis during the Late Quaternary?, Polar Science, 30, doi:10.1016/j.polar.2021.100636.

Zhang, W. L., T. Li, X. M. Fang, T. Zhang, M. D. Yan, J. B. Zan, Y. B. Yang, and D. B. B. Khatri (2021), Chronological and rock magnetic constraints on the transition of the Quaternary paleoclimate in the western Qaidam Basin, NE Tibetan Plateau, Quaternary Research, 104, 170-181, doi:10.1017/qua.2021.15.

Zhong, Y., et al. (2021), Contrasting Sensitivity of Weathering Proxies to Quaternary Climate and Sea-Level Fluctuations on the Southern Slope of the South China Sea, Geophysical Research Letters, 48(24), doi:10.1029/2021gl096433.

Extraterrestrial and Planetary Magnetism

Wickramarathna, S., R. Chandrajith, A. Senaratne, V. Paul, P. Dash, S. Wickramasinghe, and P. J. Biggs (2021), Bacterial influence on the formation of hematite: implications for Martian dormant life, International Journal of Astrobiology, 20(4), 270-284, doi:10.1017/s1473550421000124.

Fundamental Rock Magnetism and applications

Abrajevitch, A., A. P. Roberts, B. J. Pillans, and R. S. Hori (2021), Unexpected Magnetic Behavior of Natural Hematite-Bearing Rocks at Low Temperatures, Geochemistry Geophysics Geosystems, 22(12), doi:10.1029/2021gc010094.

Beguin, A., and K. Fabian (2021), Demagnetization Energy and Internal Stress in Magnetite From Temperature-Dependent Hysteresis Measurements, Geophysical Research Letters, 48(24), doi:10.1029/2021gl096147.

Dudzisz, K., M. Walter, R. Krumholz, B. Reznik, and A. Kontny (2022), Effect of cyclic loading at elevated temperatures on the magnetic susceptibility of a magnetite-bearing ore, Geophysical Journal International, 228(2), 1346-1360, doi:10.1093/gji/ggab400.

Gehring, A. U., A. Firlus, D. Koulialias, P. G. Weidler, and J. F. Loffler (2022), The Besnus transition in 4C pyrrhotite revisited, Geophysical Journal International, 228(3), 1724-1730, doi:10.1093/gji/ggab430.

Kanakiya, S., G. M. Turner, M. C. Rowe, L. Adam, and J. M. Lindsay (2021), High Remanent Magnetization Measured in Hydrothermally Altered Lavas, Geophysical Research Letters, 48(23), doi:10.1029/2021gl095732.

Knafelc, J., S. E. Bryan, M. W. M. Jones, D. Gust, G. Mallmann, H. E. Cathey, A. J. Berry, E. C. Ferre, and D. L. Howard (2022), Havre 2012 pink pumice is evidence of a short-lived, deep-sea, magnetite nanolite-driven explosive eruption, Communications Earth & Environment, 3(1), doi:10.1038/s43247-022-00355-3.

Nagy, L., W. Williams, and L. Tauxe (2021), Estimating the Effect of Cooling Rate on the Acquisition of Magnetic Remanence, Geophysical Research Letters, 48(22), doi:10.1029/2021gl095284.

Geomagnetism, Paleointensity and Records of the Geomagnetic Field

Cromwell, G., and Y. M. Zhang (2021), New Paleointensity Data From Aniakchak Volcano, Alaska, USA, Geochemistry Geophysics Geosystems, 22(12), doi:10.1029/2021gc010032.

Davis, W., and B. Buffett (2022), Inferring core processes using stochastic models of the geodynamo, Geophysical Journal International, 228(3), 1478-1493, doi:10.1093/gji/ggab412.

Diaz-Ortega, U., R. Garcia-Ruiz, M. Cervantes-Solano, A. Goguitchaichvili, R. Maciel-Pena, J. Morales-Contreras, and R. Cejudo-Ruiz (2021), implicaciones sobre el comportamiento del campo magnetico terrestre durante el Plio-Cuaternario, Revista Mexicana De Ciencias Geologicas, 38(3), 259-271, doi:10.22201/cgeo.20072902e.2021.3.1671.

Grappone, J. M., J. M. Russell, and A. J. Biggin (2021), Investigating the utility of a high-temperature Thellier-style paleointensity experimental protocol, Earth Planets and Space, 73(1), doi:10.1186/s40623-021-01558-2.

Handford, B. T., A. J. Biggin, M. M. Haldan, and C. G. Langereis (2021), Analyzing Triassic and Permian Geomagnetic Paleosecular Variation and the Implications for Ancient Field Morphology, Geochemistry Geophysics Geosystems, 22(11), doi:10.1029/2021gc009930.

Lund, S. P., M. Richardson, K. Verosub, J. King, D. Champion, and G. St-Onge (2021), Comparison and Renormalization of Holocene Paleointensity Records From Central North America (17 degrees N-51 degrees N, 205 degrees E-295 degrees E), Earth and Space Science, 8(12), doi:10.1029/2021ea001900.

Meduri, D. G., A. J. Biggin, C. J. Davies, R. K. Bono, C. J. Sprain, and J. Wicht (2021), Numerical Dynamo Simulations Reproduce Paleomagnetic Field Behavior, Geophysical Research Letters, 48(5), doi:10.1029/2020gl090544.

Muxworthy, A. R., and E. B. Baker (2021), ThellierCoolPy: A Cooling-Rate Correction Tool for Paleointensity Data, Geochemistry Geophysics Geosystems, 22(12), doi:10.1029/2021gc010145.

Rong, Z. J., et al. (2021), A New Technique to Diagnose the Geomagnetic Field Based on a Single Circular Current Loop Model, Journal of Geophysical Research-Solid Earth, 126(11), doi:10.1029/2021jb022778.

Shcherbakova, V. V., G. V. Zhidkov, V. P. Shcherbakov, I. V. Golovanova, K. N. Danukalov, and R. Y. Salmanova (2021), Ultra-Low Geomagnetic Field Intensity in the Devonian Obtained from the Southern Ural Rock Studies, Izvestiya-Physics of the Solid Earth, 57(6), 900-912, doi:10.1134/s1069351321060070.

Velle, J. H., M. H. Walczak, B. Reilly, G. St-Onge, J. S. Stoner, S. Fallon, A. C. Mix, C. Belanger, and M. Forwick (2022), High resolution inclination records from the Gulf of Alaska, IODP Expedition 341 Sites U1418 and U1419, Geophysical Journal International, 229(1), 345-358, doi:10.1093/gji/ggab479.

Venkateshwarlu, M., and K. Arora (2021), Studies of the Earth's Magnetic Field from Peninsular India: Contributions from CSIR-NGRI, Journal of the Geological Society of India, 97(10), 1135-1143, doi:10.1007/s12594-021-1842-8.

Magnetic Fabrics and Anisotropy

Anastasio, D. J., F. J. Pazzaglia, J. M. Pares, K. P. Kodama, C. Berti, J. A. Fisher, A. Montanari, and L. K. Carnes (2021), Application of anisotropy of magnetic susceptibility (AMS) fabrics to determine the kinematics of active tectonics: examples from the Betic Cordillera, Spain, and the Northern Apennines, Italy, Solid Earth, 12(5), 1125-1142, doi:10.5194/se-12-1125-2021.

Bazargan, M., H. B. Motra, B. Almqvist, S. Piazolo, and C. Hieronymus (2021), Pressure, temperature and lithological

dependence of seismic and magnetic susceptibility anisotropy in amphibolites and gneisses from the central Scandinavian Caledonides, Tectonophysics, 820, doi:10.1016/j.tecto.2021.229113.

Cao, X. W., Z. M. Sun, B. C. Huang, Y. Cao, J. L. Pei, X. Z. Ye, and S. Q. Liu (2021), The investigations of the deformation of the Great Counter Thrust (GCT) in Zedang area, South Tibet: A case study of magnetic fabric and EBSD analysis, Acta Petrologica Sinica, 37(10), 3167-3184, doi:10.18654/1000-0569/2021.10.12.

Cruz, C., H. Sant'Ovaia, M. I. B. Raposo, J. M. Lourenco, F. Almeida, and F. Noronha (2021), Unraveling the emplacement history of a Portuguese post-tectonic Variscan pluton using magnetic fabrics and gravimetry, Journal of Structural Geology, 153, doi:10.1016/j.jsg.2021.104470.

Hrouda, F., J. Franek, S. Gilder, M. Chadima, J. Jezek, S. Mrazova, M. Ponavic, and M. Racek (2022), Lattice preferred orientation of graphite determined by the anisotropy of out-of-phase magnetic susceptibility, Journal of Structural Geology, 154, doi:10.1016/j.jsg.2021.104491.

Issachar, R., T. Levi, and R. Weinberger (2022), Differentiating between remote and local strain fields near mesoscale faults by magnetic fabrics in deformed chalks, Journal of Structural Geology, 155, doi:10.1016/j.jsg.2022.104524.

Jezek, J., and F. Hrouda (2022), Startlingly strong shape anisotropy of AC magnetic susceptibility due to eddy currents, Geophysical Journal International, 229(1), 359-369, doi:10.1093/gji/ggab486.

Li, B. S., M. D. Yan, W. L. Zhang, X. M. Fang, Y. P. Yang, D. W. Zhang, C. Guan, and J. Bao (2021), Two-stage strike-slip faulting of the Altyn Tagh Fault revealed by magnetic fabrics in the Qaidam Basin, Tectonophysics, 821, doi:10.1016/j.tecto.2021.229142.

Ozkaptan, M., E. Gulyuz, B. Uzel, C. G. Langereis, A. A. Ozacar, and N. Kaymakci (2021), Deformation in SW Anatolia (Turkey) Documented by Anisotropy of Magnetic Susceptibility Data, Tectonics, 40(12), doi:10.1029/2021tc006882.

Sangode, S. J., S. Tembhurne, R. Mahajan, K. Deenadayalan, D. C. Meshram, A. N. Dongre, A. R. Bhagat, and K. V. V. Satyanarayana (2022), Magnetic fabrics and magnetic mineralogical variations in Lava Channel: An example from the Deccan Volcanic Province, India, Journal of Earth System Science, 131(1), doi:10.1007/s12040-021-01769-x.

Test, C. R., and E. Zanella (2021), Rock Magnetic Signature of Heterogeneities Across an Intraplate Basal Contact: An Example From the Northern Apennines, Geochemistry Geophysics Geosystems, 22(12), doi:10.1029/2021gc010004.

Weinberger, R., G. I. Alsop, and T. Levi (2022), Magnetic fabrics as strain markers in folded soft-sediment layers, Journal of Structural Geology, 155, doi:10.1016/j.jsg.2022.104513.

Magnetic Microscopy

Pastore, Z., P. Lelievre, S. A. McEnroe, and N. S. Church (2022), 3D Joint Inversion of Scanning Magnetic Microscopy Data, Geophysical Research Letters, 49(1), doi:10.1029/2021gl096072.

Wu, J. J., Q. Q. Zhi, X. H. Deng, X. C. Wang, X. D. Chen, Y. Zhao, and Y. Huang (2022), Deep Gold Exploration with SQUID TEM in the Qingchengzi Orefield, Eastern Liaoning, Northeast China, Minerals, 12(1), doi:10.3390/min12010102.

Magnetic Mineralogy and Petrology

Bian, G., O. Ageeva, A. Recnik, G. Habler, and R. Abart (2021), Formation pathways of oriented magnetite microinclusions in plagioclase from oceanic gabbro, Contributions to Mineralogy and Petrology, 176(12), doi:10.1007/s00410-021-01864-8.

Chakoumakos, B. C., and J. B. Parise (2021), Probing Phase Transitions and Magnetism in Minerals with Neutrons, Elements, 17(3), 181-188, doi:10.2138/gselements.17.3.181.

Gorbatova, E. A., V. V. Kholodnov, B. I. Pirogov, M. S. Kolkova, and E. S. Shagalov (2021), Solid-Phase Transformations of Titanomagnetite and Ilmenite during Oxidizing Roasting of Disseminated Titanomagnetite-Ilmenite Ore at the Medvedevskoe Deposit and Certain Geological Events (Southern Urals), Geology of Ore Deposits, 63(5), 431-453, doi:10.1134/s1075701521040036.

Li, Y., A. E. Rubin, and W. B. Hsu (2021), Formation of metallic-Cu-bearing mineral assemblages in type-3 ordinary and CO chondrites, American Mineralogist, 106(11), 1751-1767, doi:10.2138/am-2021-76891751.

Meszarosova, N., R. Skala, P. Mikysek, and M. Drabek (2021), Miscibility between synthetic FeS and TiS: An insight into the phase relations in natural Ti-bearing iron monosulfides, Journal of Geosciences, 66(4), 215-225, doi:10.3190/jgeosci.334.

Noguchi, T., M. Yasutake, A. Tsuchiyama, A. Miyake, M. Kimura, A. Yamaguchi, N. Imae, K. Uesugi, and A. Takeuchi (2021), Mineralogy of fine-grained matrix, fine-grained rim, chondrule rim, and altered mesostasis of a chondrule in Asuka 12169, one of the least altered CM chondrites, Polar Science, 29, doi:10.1016/j.polar.2021.100727.

Ren, M., and B. Jones (2021), Modern authigenic amorphous and crystalline iron oxyhydroxides in subsurface Ordovician dolostones (Jinan, North China Block): Biomineralization and crystal morphology, Sedimentary Geology, 426, doi:10.1016/j.sedgeo.2021.106044.

Yang, M. J., X. L. Liang, Y. Li, H. P. He, R. L. Zhu, and Y. Arai (2021), Ferrihydrite Transformation Impacted by Adsorption and Structural Incorporation of Rare Earth Elements, Acs Earth and Space Chemistry, 5(10), 2768-2777, doi:10.1021/acsearthspacechem.1c00159.

Yin, S., R. Wirth, H. P. He, C. Q. Ma, J. Y. Pan, J. Q. Xing, J. N. Xu, J. L. Fu, and X. N. Zhang (2022), Replacement of magnetite by hematite in hydrothermal systems: A refined redox-independent model, Earth and Planetary Science Letters, 577, doi:10.1016/j.epsl.2021.117282.

Magnetotactic Bacteria

Chen, H. T., J. H. Li, L. F. Wu, and W. J. Zhang (2021a), Morphological and phylogenetic diversity of magnetotactic bacteria and multicellular magnetotactic prokaryotes from a mangrove ecosystem in the Sanya River, South China, Journal of Oceanology and Limnology, 39(6), 2015-2026, doi:10.1007/s00343-021-0491-5.

Chen, S., K. X. Cui, W. Y. Zhang, Y. C. Zhao, T. Xiao, H. M. Pan, W. C. Zhang, and L. F. Wu (2021b), Observations on a magnetotactic bacteria-grazing ciliate in sediment from the intertidal zone of Huiquan Bay, China, Journal of Oceanology and Limnology, 39(6), 2053-2062, doi:10.1007/s00343-021-1011-3.

Cui, K. X., W. Y. Zhang, J. Liu, C. Xu, Y. C. Zhao, S. Chen, H. M. Pan, T. Xiao, and L. F. Wu (2021), Characterization and diversity of magnetotactic bacteria from sediments of Caroline Seamount in the Western Pacific Ocean, Journal of Oceanology and Limnology, 39(6), 2027-2043, doi:10.1007/s00343-021-0029-x.

Qian, X. X., et al. (2021), How light affect the magnetotactic behavior and reproduction of ellipsoidal multicellular magnetoglobules?, Journal of Oceanology and Limnology, 39(6), 2005-2014, doi:10.1007/s00343-021-0493-3.

Zhang, T. W., H. T. Xu, J. Liu, Y. X. Pan, and C. Q. Cao (2021), Determination of the heating efficiency of magnetotactic bacteria in alternating magnetic field, Journal of Oceanology and Limnology, 39(6), 2116-2126, doi:10.1007/s00343-021-1071-4.

Paleomagnetism

Brooks, K. I., P. J. A. McCausland, and J. W. F. Waldron (2021), Paleolatitude and tectonic rotations of the Early Carboniferous Fountain Lake Group, Cobequid Highlands, Nova Scotia, Canada, Canadian Journal of Earth Sciences, 58(10), 1103-1115, doi:10.1139/cjes-2020-0165.

Cantalejo, B., K. T. Pickering, K. G. Miller, and C. M. Niocaill (2021), Chasing the 400 kyr pacing of deep-marine sandy submarine fans: Middle Eocene Ainsa Basin, Spanish Pyrenees, Journal of the Geological Society, 178(1), doi:10.1144/jgs2019-173.

Cocks, L. R. M., and T. H. Torsvik (2021), Ordovician palaeogeography and climate change, Gondwana Research, 100, 53-72, doi:10.1016/j.gr.2020.09.008.

Condie, K. C. (2021), Revisiting the Mesoproterozoic, Gondwana Research, 100, 44-52, doi:10.1016/j.gr.2020.08.001.

Djeutchou, C., M. O. de Kock, H. Wabo, C. E. Gaitan, U. Soderlund, and A. P. Gumsley (2021), Late Paleoproterozoic mafic magmatism and the Kalahari craton during Columbia assembly, Geology, 49(11), 1375-1380, doi:10.1130/g48811.1.

Dong, Y. P., S. S. Sun, M. Santosh, J. Zhao, J. P. Sun, D. F. He, X. H. Shi, B. Hui, C. Cheng, and G. W. Zhang (2021), Central China Orogenic Belt and amalgamation of East Asian continents, Gondwana Research, 100, 131-194, doi:10.1016/j.gr.2021.03.006.

Gao, L., J. L. Pei, Y. Zhao, Z. Y. Yang, T. R. Riley, X. C. Liu, S. H. Zhang, and J. M. Liu (2021), New Paleomagnetic Constraints on the Cretaceous Tectonic Framework of the Antarctic Peninsula, Journal of Geophysical Research-Solid Earth, 126(11), doi:10.1029/2021jb022503.

Guan, C., et al. (2021), Paleomagnetic and Chronologic Data Bearing on the Permian/Triassic Boundary Position of Qamdo in the Eastern Qiantang Terrane: Implications for the Closure of the Paleo-Tethys, Geophysical Research Letters, 48(6), doi:10.1029/2020gl092059.

Luoto, T., J. Salminen, and K. Obst (2021), Revisiting mafic dykes of Bornholm-Implications for Baltica in supercontinent Nuna at 1.3 Ga, Precambrian Research, 367, doi:10.1016/j.precamres.2021.106444.

Malaguti, A. B., M. Rosi, M. Pistolesi, F. Speranza, and M. Menzies (2022), The contribution of palaeomagnetism, tephrochronology and radiocarbon dating to refine the last 1100 years of eruptive activity at Vulcano (Italy), Bulletin of Volcanology, 84(1), doi:10.1007/s00445-021-01515-7.

Metelkin, D. V., A. I. Chernova, V. A. Vernikovsky, N. E. Mikhaltsov, and V. V. Abashev (2021), The Rock Magnetic Portrait of the Devonian Section of Stolb Island (Lena River Delta), Doklady Earth Sciences, 501(1), 906-911, doi:10.1134/s1028334x2111009x.

Metelkin, D. V., V. V. Abashev, V. A. Vernikovsky, and N. E. Mikhaltsov (2021), Paleomagnetic Evidence for the Iceland Plume Paleogeographic Stationarity and Early Cretaceous Manifestation in the High Arctic, Doklady Earth Sciences, 501(2), 1015-1019, doi:10.1134/s1028334x21120072.

Mostafa, R., W. Hagag, Z. Hamimi, A. R. Fowler, and I. El-Hemaly (2022), Paleomagnetism as a geochronological gauge for deformational events: Insights from the Najd-related Nugrus Shear Zone, Northern Nubian Shield, Journal of Asian Earth Sciences, 223, doi:10.1016/j.jseaes.2021.104988.

Temporim, F. A., U. D. Bellon, M. Domeier, R. I. F. Trindade, M. S. D'Agrella, and E. Tohver (2021), Constraining the Cambrian drift of Gondwana with new paleomagnetic data from post-collisional plutons of the Aracuai orogen, SE Brazil, Precambrian Research, 359, doi:10.1016/j.precamres.2021.106212.

Todrani, A., F. Speranza, N. D'Agostino, and B. Zhang (2022), Post-50 Ma Evolution of India-Asia Collision Zone From Paleomagnetic and GPS Data: Greater India Indentation to Eastward Tibet Flow, Geophysical Research Letters, 49(1), doi:10.1029/2021gl096623.

Wabo, H., M. O. De Kock, N. J. Beukes, and V. S. Hegde (2022), Palaeomagnetism of the uppermost carbonate units of the Purana basins in southern India: new demagnetization results from the Kaladgi and Bhima basins, Karnataka, Geological Magazine, 159(2), 269-278, doi:10.1017/s0016756820001181.

Zhang, W. L., D. W. Zhang, X. M. Fang, T. Zhang, C. H. Chen, and M. D. Yan (2020b), New paleomagnetic constraints on rift basin evolution in the northern Himalaya mountains, Gondwana Research, 77, 98-110, doi:10.1016/j.gr.2019.07.008.

Zhao, Q., B. C. Huang, Z. Y. Yi, and P. F. Xue (2021), High-Resolution Petrographic Evidence Confirming Detrital and Biogenic Magnetites as Remanence Carriers for Zongpu Carbonates in the Gamba Area, South Tibet, Frontiers in Earth Science, 9, doi:10.3389/feart.2021.713469.

Stratigraphy

Day, M. O., J. Ramezani, R. E. Frazer, and B. S. Rubidge (2022), U-Pb zircon age constraints on the vertebrate assemblages and palaeomagnetic record of the Guadalupian Abrahamskraal Formation, Karoo Basin, South Africa, Journal of African Earth Sciences, 186, doi:10.1016/j.jafrearsci.2021.104435.

Green, T., S. P. Slotznick, P. Jaqueto, T. D. Raub, E. Tohver, T. E. Playton, P. W. Haines, J. L. Kirschvink, R. M. Hocking, and P. Montgomery (2021), High-Resolution Late Devonian Magnetostratigraphy From the Canning Basin, Western Australia: A Re-Evaluation, Frontiers in Earth Science, 9, doi:10.3389/feart.2021.757749.

Haneda, Y., and M. Okada (2022), A record of the lower Mammoth geomagnetic polarity reversal from a marine succession in the Boso Peninsula, central Japan, Geophysical Journal International, 228(1), 461-476, doi:10.1093/gji/ggab352.

Jimenez, G., H. Garcia-Delgado, and J. W. Geissmanz (2021), Magnetostratigraphy and magnetic properties of the Jurassic to Lower Cretaceous Giron Group (northern Andes, Colombia), Geosphere, 17(6), 2172-2196, doi:10.1130/ges02186.1.

Kanamatsu, T., K. Ikehara, and K. H. Hsiung (2022), Stratigraphy of deep-sea marine sediment using paleomagnetic secular variation: Refined dating of turbidite relating to giant earthquake in Japan Trench, Marine Geology, 443, doi:10.1016/j.margeo.2021.106669.

Kodama, K. P. (2021), Combined Magnetostratigraphy From Three Localities of the Rainstorm Member of the Johnnie Formation in California and Nevada, United States Calibrated by Cyclostratigraphy: A 13 R/Ma Reversal Frequency for the Ediacaran, Frontiers in Earth Science, 9, doi:10.3389/feart.2021.764714.

Li, H. Y., et al. (2022), Astrochronologic calibration of the Shuram carbon isotope excursion with new data from South China, Global and Planetary Change, 209, doi:10.1016/j.gloplacha.2022.103749.

Lodowski, D. G., A. Pszczolkowski, O. Szives, I. Fozy, and

J. Grabowski (2022), Jurassic-Cretaceous transition in the Transdanubian Range (Hungary): integrated stratigraphy and paleomagnetic study of the Harskut and Lokut sections, Newsletters on Stratigraphy, 55(1), 99-135, doi:10.1127/nos/2021/0656.

Ma, X. D., et al. (2022), High-resolution late Pliocene-quaternary magnetostratigraphy of the Yinchuan Basin, NE Tibetan Plateau, Quaternary International, 607, 120-127, doi:10.1016/j.quaint.2021.09.009.

Perini, S., G. Muttoni, E. Monesi, R. T. Melis, and M. Mussi (2021), Magnetochronology and age models of deposition of the Melka Kunture stratigraphic sequence (Upper Awash, Ethiopia) and age assessments of the main archeological levels therein contained, Quaternary Science Reviews, 274, doi:10.1016/j.quascirev.2021.107259.

Zhang, W. L., et al. (2020a), Magnetostratigraphic constraints on the age of the Hipparion fauna in the Linxia Basin of China, and its implications for stepwise aridification, Palaeogeography Palaeoclimatology Palaeoecology, 537, doi:10.1016/j.palaeo.2019.109413.

Zhao, Z. X., W. Shi, Y. Yang, M. T. Cai, C. F. Liu, X. B. Liu, T. Y. Wang, Y. F. Zhao, and Q. Yang (2022), Late Cenozoic magnetostratigraphy and paleoenvironmental change in the northeastern Tibetan Plateau: Evidence from a drill core in the Wuwei Basin, NW China, Journal of Asian Earth Sciences, 224, doi:10.1016/j.jseaes.2021.105023.

Zykin, V. S., S. Zykina, D. G. Malikov, L. G. Smolyaninova, and O. B. Kuzmina (2021), Lower-Middle Pleistocene Stratigraphy of the Southern West Siberian Plain: New Data, Russian Geology and Geophysics, 62(12), 1359-1372, doi:10.2113/rgg20204218.

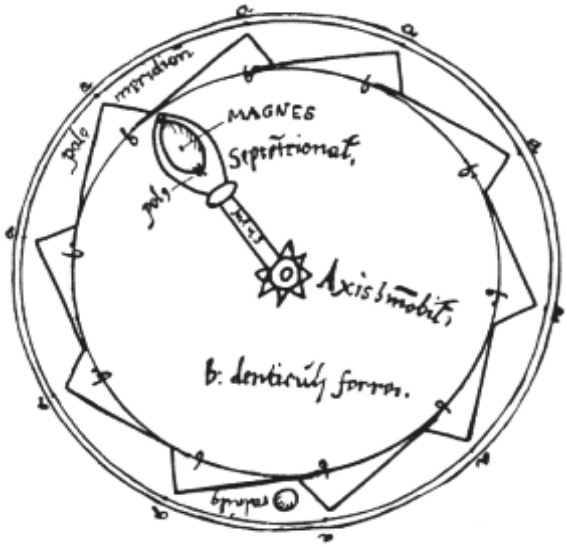

cont'd. from pg. 1...

2. Switching field angular dependence and benefits of the high alternating field

The most obvious benefit of the higher AF achievable with the magnetic-core design is identification of higher coercivity components than is possible with conventional demagnetizers (Figure 1c). Similarly, the new design can impart an ARM on higher coercivity particles, which is particularly important since most of the higher coercivity portion of a typical ARM is of limited use for anisotropy of magnetic remanence, coercivity distribution, and relative paleointensity (RPI). A condition to strive to meet for most measurements of laboratory imparted remanence is full activation, so that all magnetic grains in the sample or in a discrete coercivity or unblocking temperature range have the ability to contribute to the magnetization. Full activation is important because it's a requirement (1) for a set of directional measured ARMs or TRMs to be describable with a tensor, (2) for a valid comparison between ARMs and NRMs for relative paleointensity, and (3) for comparison of ARMs in different coercivity ranges to estimate magnetic grain size distributions (Finn and Coe, 2020).

The case for TRM is simple. Regardless of their orientations, all particles in a rock with blocking temperature T_b are fully activated when the temperature is above T_b because they all have the potential of contributing to the remanence as they cool below T_b. For ARM, however, the activation of a particle is dependent on coercivity as well as the angle between the applied field and particle easy axis. In consequence, the condition of full activation may only be achieved with an applied field significantly larger than the particle coercivity. The property of full activation is rooted in the nature of switching-field angular dependence. Aharoni's (1986) switching-field relation (equation 1 and Figure 2), formulated for incoherently switching uniaxial single-domain grains (e.g., vortex state), describes reasonably well the behavior of perhaps most, magnetite-bearing rocks (Finn and Coe, 2020, and references therein). For our purposes, considering an ensemble of such magnetic grains with long (= easy) axes distributed in all directions over the sphere, it is most usefully expressed as

$$C_m(\Theta) = AF\,(1 - \alpha \sin^2(\Theta))^{1/2} \qquad \text{Equation 1}$$

where $C_m(\Theta)$ is the maximum coercivity particle oriented with its easy axis at an angle Θ to the AF that can be switched (i.e., activated) by that AF. Experimental estimates of the parameter α fall mainly between 0.80 and 0.95 (Stephenson and Shao 1994; Madsen 2002; 2003; 2004), larger values requiring higher peak-AF ARMs to fully activate grains of a given coercivity. For the upper limit $\alpha = 1$ full activation would not be possible at all because it would require an infinite AF to switch grains with long axes perpendicular to the AF direction.

The higher the AF used to impart an ARM, the higher the activation line dividing fully from partially activated particles (Figure 2b). Another way to look at this phe-

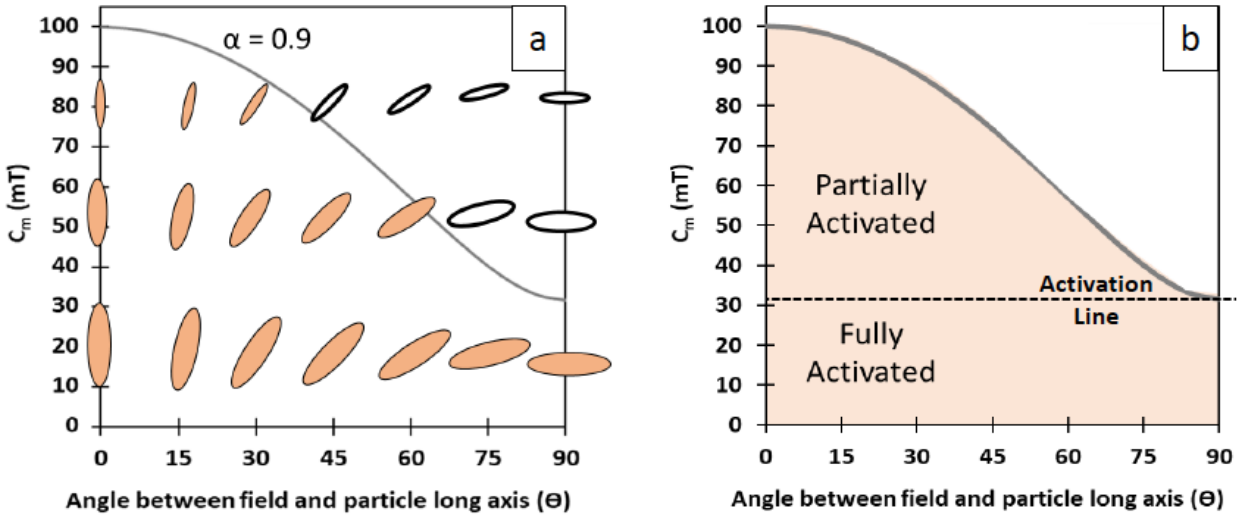

Figure 2. Coercivity and orientation distribution of particles activated by a 100 mT AF. These particles are available to be biased by the presence of weak direct field when imparting an ARM. The curve in (a) uses the incoherent switching field angular dependence proposed by Aharoni (1986) to plot the maximum coercivity particle (C_m) activated as a function of angle made between the AF and particle long axis (Finn and Coe 2020). A switching field parameter α= 0.9 is used which is thought to be representative of a wide range of magnetite particle sizes. Particles below this line are activated by the 100 mT ARM, and those above the line are untouched. The plot in (b) shows the activated region under the curve (shaded) divided into partially and fully activated zones. The condition of full activation requires that all particles of a given coercivity range are activated regardless of their orientation.

nomenon is that an ARM will only be fully activating over a given coercivity range when the peak-AF that generated it is sufficiently large so that its resolved easy-axis component can exceed the coercivity of particles oriented at high angles to the AF. In addition, this switching effect also results in a range of particle coercivities locking in during any given small segment of AF decay, ΔAF. Because of this, the magnetization acquired by turning the direct bias on for only a small window of the AF decay (i.e., pARM) will be carried by particles with a wide range of coercivities extending far below the pARM window.

Figure 3 shows the expected influence of change in activation degree on relative paleointensity measurements for various kinds of samples. Figure 3a utilizes 3-axis AF demagnetization in a Sapphire SI-4 instrument in 10 mT steps up to 160 mT of an ignimbrite sample's NRM (almost entirely TRM) and of two ARMs given to the same sample as the AF decayed from a peak of 175 mT in the Sapphire and from 450 mT in the Schillinger demagnetizer. The 160 mT demagnetization step was subtracted from the NRM, ARM_{175} and ARM_{450} to ensure the same remanence coercivity portion is compared from each demagnetization. The ratio of NRM remaining to ARM remaining during progressive demagnetization is plotted in Figure 3a for both ARMs tested. As expected, the NRM/ARM_{175} ratio is initially larger and proceeds to skyrocket as AF demagnetization progresses beyond the range of full activation (e.g., 55 mT for α= 0.9, from equation 1) where less ARM was activated. ARM_{450}, however, is fully activated over a much larger coercivity range, so the NRM/ARM_{450} ratio in Figure 3a does not blow up, and we conclude that the 450 mT ARM is inherently more suitable for RPI estimation.

We further suggest that the large dispersion in Yu's (2010) ARM RPI determinations on synthetic SD magnetite samples may also have been because of partial activation (Figure 3b). We find similar large rises in NRM/ARM during AF demagnetization in a range of other rock types (Figure 3c and d). Yu (2010) observed that the ratio of TRM to saturation isothermal remanence (SIRM) was more stable and reliable as a paleofield proxy than the TRM/ARM ratio. This observation may have been in large part due to the SIRMs (ARMs) being fully (partially) activating, rather than an inherent closer similarity between IRMs and TRMs. Furthermore, calibration of TRM to ARM for a given direct bias intensity requires both remanences are fully activating. This condition was satisfied in a seminal paper on TRM/ARM calibration through clever application of a static direct bias in the presence of a tumbling AF (Stephenson and Collinson 1974).

3. Model description

The modelling that follows compares the incoherent switching field behavior described by Aharoni (1986) with the classic Stoner-Wohlfarth (SW) behavior (Stoner & Wohlfarth 1948). The primary differences are that SW behavior is characterized by the field being most effective at a 45° to the particle long axis, while incoherent switching is most effective with a field aligned parallel to the particle long axis. Importantly, a given field application is far closer to fully activating when an ensemble of SW is considered rather than incoherently switching particles.

The model contains 1000 orientations that uniaxial particles could have (termed particle orientations). Each particle orientation can be considered to have an infinite number of particles with an even coercivity distribution that, depending on which model is shown, may be variably restricted to a certain coercivity range. Whether an individual particle within a particle orientation gets acti-

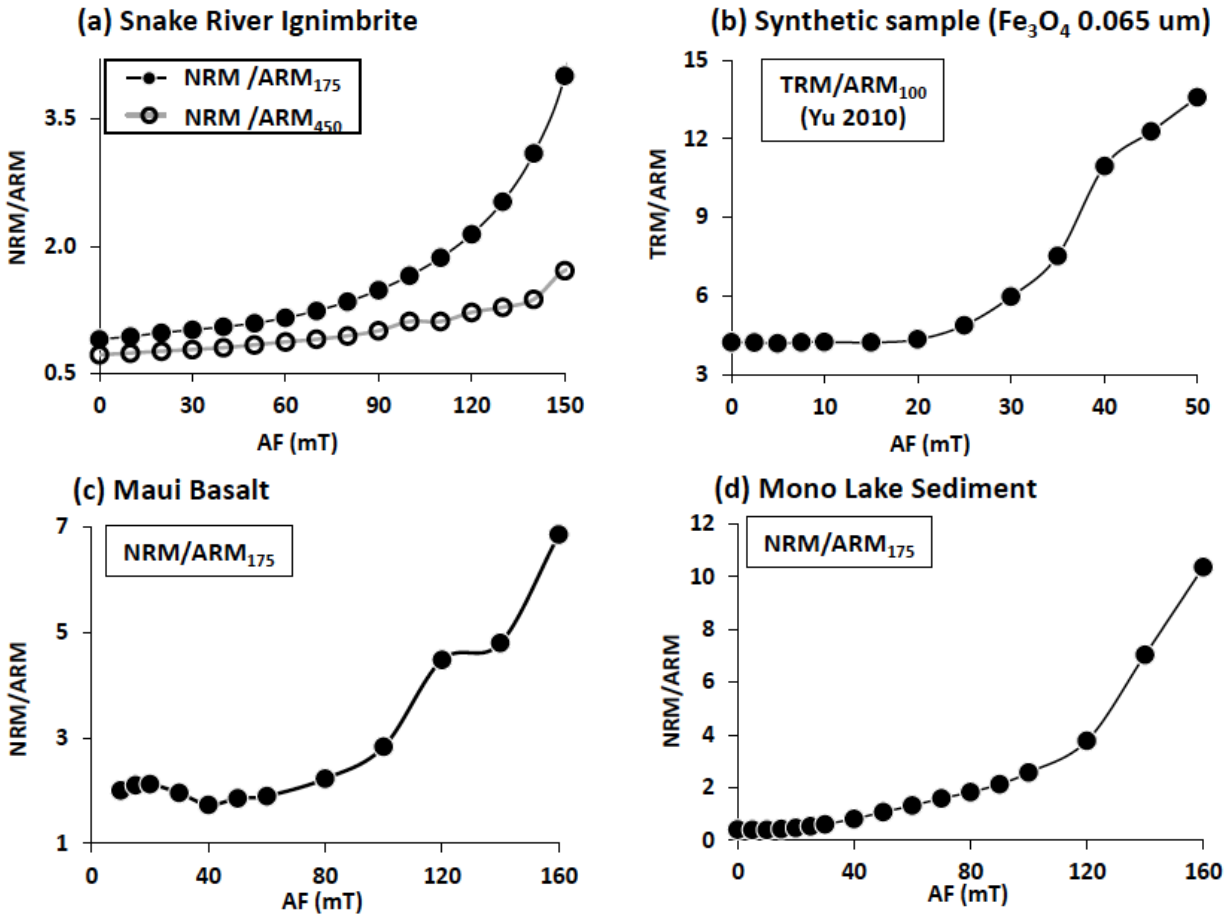

Figure 3. Effect of partial activation on ARM relative paleointensity determinations (see text, section 2). (a) Ratios of NRM (dominantly a TRM) vs ARM during progressive demagnetization are shown for a SR-type glassy ignimbrite sample. Two ARMs were compared, one given to a peak field of 175 mT and another to 450 mT using the Schillinger demagnetizer. The 160 mT step was initially subtracted off all data to remove the contribution from higher coercivity particles (160+ mT). The large ARM_{450} provided by the Schillinger demagnetizer eliminates the unrealistic rise in the ratio due to incomplete activation, enabling more reliable RPI estimates. (b) The TRM/ARM_{100} ratio for a synthetic sample created from magnetite powder with a mean grain size of 0.065 µm (Yu, 2010). NRM/ARM_{175} ratio for (c) a Maui basalt lava sample and (d) a Mono Lake sediment sample. The dramatic rise in ratios in b, c and d are also consistent with the expectation that the ARM is less activated at higher coercivities, whereas TRM and detrital remanence are fully activating throughout the entire coercivity range.

vated by a given AF depends on the particle's coercivity, orientation of its long axis relative to the AF, and on the strength of the AF. If a uniaxial particle is activated by a pure AF, it's moment gets set to zero. In contrast, if it is activated by an AF in the presence of a small biasing field, then the probability of that particle's moment choosing the stable position closer to the field direction is proportional to the resolved component of the direct biasing field along the particle's long axis (Stephenson 1983).

4. Aharoni (incoherent) vs Stoner-Wohlfarth (coherent) switching behavior

The angular dependence of coercivity is an important property that needs consideration in designing paleomagnetic instruments and laboratory experiments, and interpreting results. To this end, the classic Stoner-Wohlfarth switching behavior is commonly utilized for modelling and interpretation of a variety of experiments such as IRM acquisition curves, FORCs, NRM demagnetization, etc. However, the last ~30 years have seen occasional and mostly overlooked reports of experimental results that cannot be explained by the SW theory and, instead, are better reproduced assuming incoherent switching behavior (Stephenson and Shao 1994; Madsen 2002; 2003; 2004; Milne and Dunlop 2006; Finn and Coe 2020).

Similarly, though we don't model it here, the dramatic rise in NRM/ARM ratio documented in Figure 3 is better explained by incoherent Aharoni-like switching (equation 1) than by the more fully activating SW behavior. Instead, we present an even more robust test of switching behavior by comparing the progressive demagnetization of two variably sized ARMs. Figure 4a depicts the strong triaxial ARM anisotropy measured on the ignimbrite sample. Note that the principal anisotropy directions coincidentally, and for our demonstration, fortunately align near the sample axes. To test for switching behavior, we applied and progressively demagnetized in turn an ARM of 175 and 450 mT given along each sample axis (i.e., x, y, and z).

Figure 4b shows for each sample axis the ratio of ARM_{450} / ARM_{175} removed in 10 mT windows from 0 to 160 mT. The dramatic increase in ARM_{450} / ARM_{175} ratio

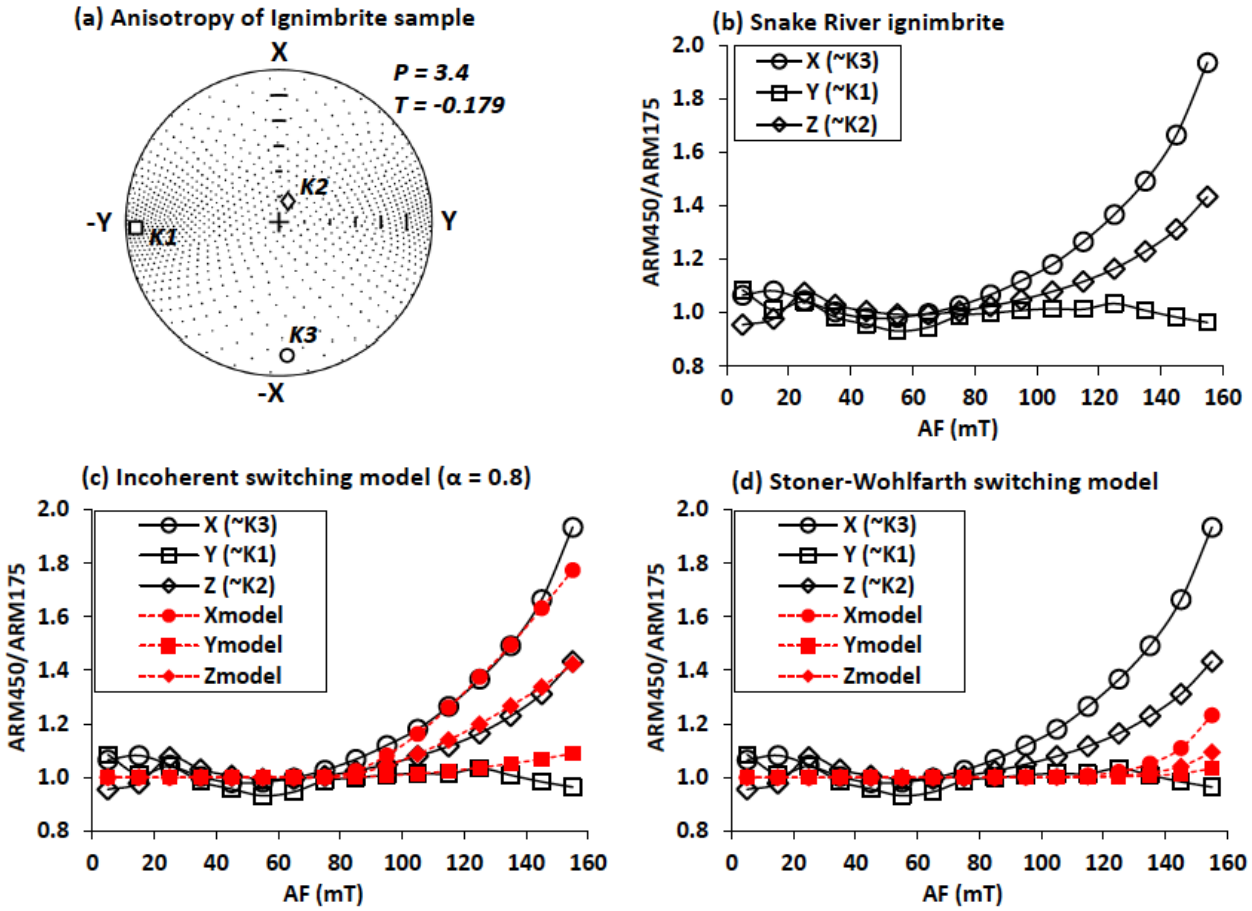

Figure 4. (a) Stereonet showing the measured ARM anisotropy of the SR-Type ignimbrite sample from Figure 3a. Size (P= 3.4), shape (T= -0.179) and orientation information are represented by a set of particle axes (black dots) that are associated with an orientation tensor (Jezek and Hrouda 2002) identical to the measured ARM anisotropy. Note the coincidentally close proximity of the sample and anisotropy axes. (b) Ratio of ARM_{450} removed to ARM_{175} removed in 10 mT windows from 0-10 mT up to 150-160 mT. ARMs were imparted in the x, y, and z sample directions, and each demagnetized with a 3-axis static AF (see text for more detail). (c & d) The exact experiment from (b) was modelled using the input anisotropy from (a) with an incoherent (c) or coherent (d) switching field behavior. The incoherent switching angular dependence (c) does a significantly better job at reproducing the measured results when compared to the coherent (Stoner-Wohlfarth model) switching behavior. Improvement to the fit shown can be obtained by consideration of a range of switching behaviors, rather then a single behavior as shown in (c).

relates directly to the decreasing activation in ARM_{175}, and is strongly dependent on ARM orientation relative to the sample anisotropy (Figure 4b). The largest and smallest rises occur when the ARMs are given near the minimum (K_3) and maximum (K_1) anisotropy directions, respectively. This observation relates to the anisotropy of activated grain concentration (Finn and Coe 2020), whereby the ARM_{175} given along K_3 is less activated then the exact same ARM_{175} given along K_1. This explanation pertains most directly to the incoherent switching behavior. The SW behavior, in contrast, suffers less from partial activation and would see far less of a difference between ARM_{450} and ARM_{175}.

We modelled the exact experiment shown in Figure 4b using incoherent and SW switching, an even coercivity distribution from 0 – 175 mT and the input anisotropy from Figure 4a. We found the incoherent switching model (Figure 4c) using an α equal to 0.8 matches the results well, while as expected, the SW model doesn't agree at all. Note that the sample has a coercivity dependent degree of anisotropy, where the model input we used (P= 3.4) is on the high end of the range of measured results. Reduction of the degree of modelled input anisotropy results in the best fit α (Figure 4c) migrating from 0.8 to closer to 1. So our estimate of α= 0.8 is probably on the low end. Furthermore, assuming a single alpha value for all particles in a sample is likely an oversimplification. Not surprisingly, we can better match these results (not shown) if we assume a distribution of α with an average of ~0.8 or 0.85, rather than a single α value for all particles.

5. Benefit of the transverse AF

We can also apply the concept of full activation to the removal of remanence. In this case, the best practice for separating magnetic components during demagnetization is to progressively remove only fully activated portions of remanence at each demagnetization step, which is best done with a tumbling AF. When restricted to using only a static AF, one can approximate a tumble by applying the AF in a larger number of orientations. One of the major benefits of the Schillinger design is the transverse orientation of the AF relative to the demagnetizer borehole. With this transverse field, a simple two-rotation axis sample handler can position the sample such that any arbitrary field orientation is obtainable. This flex-

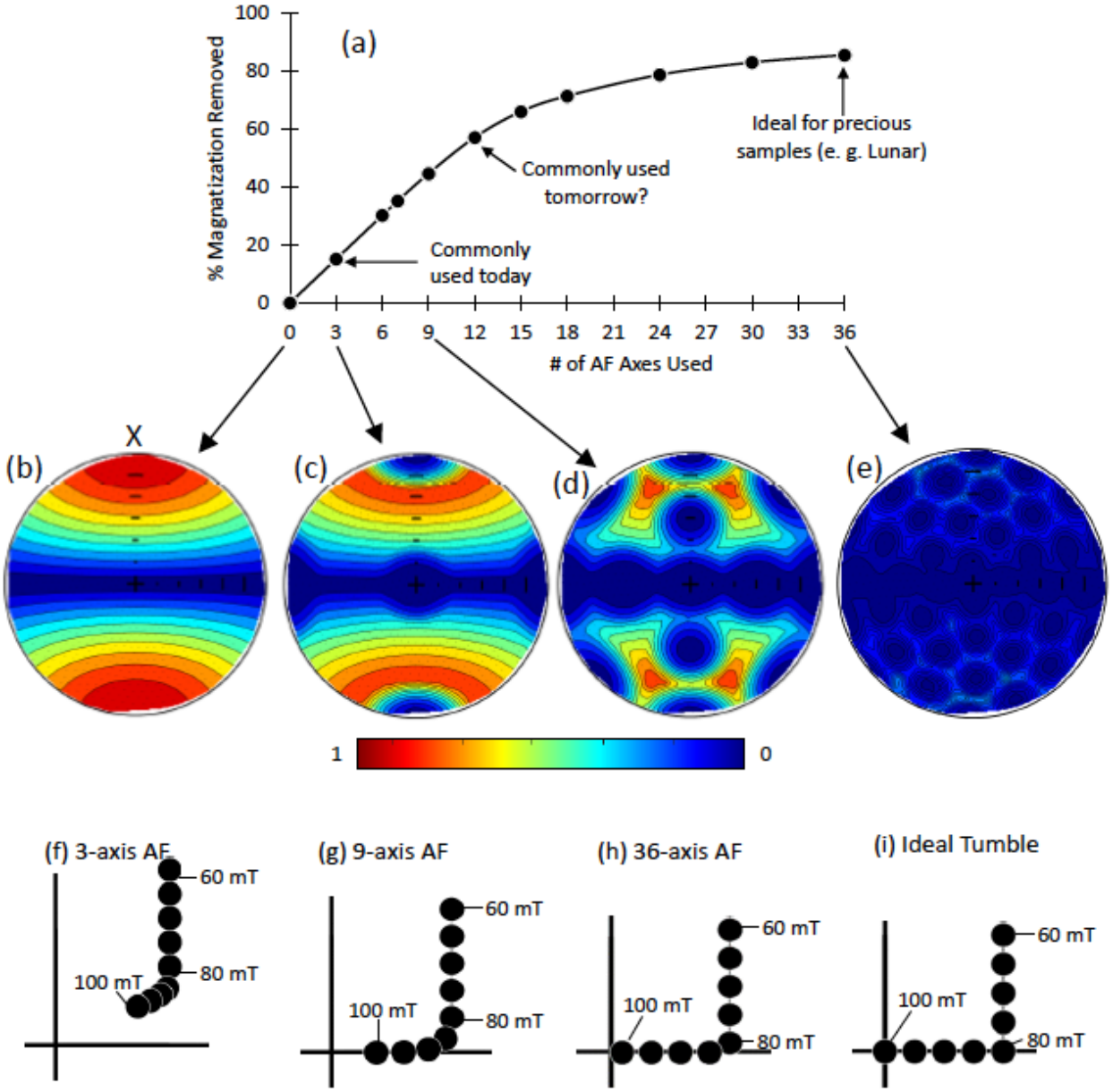

Figure 5. Modelled results comparing demagnetization efficiency with number of AF axes used per step. (a) Plot showing percentage of total ARM removed using a 100 mT AF and various demagnetization schemes (i.e., number of AF axes). The modelled uses an incoherent switching behavior with a switching parameter (α) equal to 1. It is isotropic with an even coercivity distribution entirely contained within the 90-100 mT range. Particle magnetization-orientation plots (see text) show the original magnetization state (b) and that after various demagnetization procedures (b-e). (f-i) Modelled demagnetization of two-component ARMs, where the lower and higher coercivity components are contained between 0-80 mT and 80-100 mT, respectively. Results in (a-i) collectively suggest it is worthwhile to use more than three AF axes for routine demagnetization, and perhaps 10's of AF axes for important specimens (i.e. Lunar samples).

ibility in AF direction is essential if one wishes to employ more than three AF directions at each step level, and better approximate a tumbling AF in an automated measuring system. In the section that follows we explore through simple modelling the benefits of increasing the number of AF directions used during progressive demagnetization of remanence.

5.1 How Many AF axes should be used for demagnetization?

Figure 5a shows the model results of demagnetizing a fully activating ARM using various AF demagnetization schemes, each time with a peak AF intensity of 100 mT. The Y-axis plots the percentage of the total magnetization removed from a set of AF applications, and the X-axis lists the number of AF axes used in the procedure. The model is isotropic, has an even coercivity distribution restricted to the 90-100 mT, and following the seminal earlier treatment of this multi-axis AF demagnetization problem by McFadden (1981), uses an α equal to 1.

Magnetization-orientation (M-O) plots are shown for the undemagnetized ARM and partially demagnetized ARM using various numbers of applied AF directions (Figures 5b-5e). The color-shading in the M-O plots contour the net magnetization (summed over all coercivities) of each of the 1000 particle orientations in the model. It is notable that the 3-axis static AF method removes <20% of the sample's magnetization, which means that

>80% of the magnetization carried by particles in the 90-100 mT coercivity range, would smear into a higher AF (>100 mT) segment of a progressive demagnetization.

Figure 5f-i compare models of progressive AF demagnetizations of a sample containing two orthogonal components of fully activating ARM within the 0-80 and 80-100 mT coercivity ranges, respectively (see Figure 5 caption for more details). Increase in the number of AF axes considerably improves the separation of magnetic components. Collectively, these results suggest one should choose ~9 AF axes (time permitting) for regular demagnetization on typical samples, and a scheme involving a much larger number of AF axes (e.g., n = 36) for more important specimen such as Lunar samples.

It is worth noting that real tumble AF demagnetizers are far from ideal. They do not fully account for unwanted ARM bias in the AF waveform. Additionally, unless they employ the important self-reversing rotation feature described by Wilson and Lomax (1972), they may suffer from unwanted rotational remanence acquisition. At least with the static AF method, these unwanted remanence acquisitions are predictable, their origin can be uniquely determined (e.g., ARM or GRM), and they can be excluded with careful experimental design and possibly utilized for a free estimate of magnetic anisotropy (Stephenson 1993; Finn et al 2021).

6. Path forward

The take-home message is that there is great potential for improving our everyday paleomagnetic methods by adopting the Schillinger demagnetizer design along with a two-rotation axis sample handler. This is particularly true given the recent recognition of the importance of fully activating ARMs. Additionally, most magnetite particles experience incoherent switching behavior, and thus are more difficult to fully activate then SW particles. The upgrade to the Schillinger design, however, is not available for purchase off the shelf, and most paleomagnetic laboratories do not have the capability to build their own instruments. As with other major infrastructure projects, this improvement to paleomagnetic instrumentation could benefit from a community, rather than individually led effort.

7. Acknowledgements

We would like to thank the National Environmental Research Council in the UK for funding the first authors contribution to this work (NERC grants: NE/S002235/1 and NE/G005672/1 to the University of Leicester) and the Deutsche Forschungsgemeinschaft for funding the SushiBar with grant GI712/1-1. We also thank Dario Bilardello for inviting us to write this article, and his help and patience during its construction.

References

Aharoni, A. (1986). Angular dependence of nucleation field in magnetic recording particles. IEEE transactions on magnetics, 22(3), 149-150.

Finn, D., & Coe, R. (2020). Consequences of switching field angular dependence for applications of anhysteretic remanent magnetization. Physics of the Earth and Planetary Interiors, 305, 106507.

Finn, D., Gilder, S., Coe, R., & Pike, A. (2021). Effect of gyroremenance on relative paleointensity estimates applied to ignimbrite. Physics of the Earth and Planetary Interiors, 318, 106769.

Madsen, K. N. (2002). Angular dependence of switching field measured on maghemite recording particles. Journal of magnetism and magnetic materials, 241(2-3), 220-227.

Madsen, K. N. (2003). A reversed gyromagnetic effect in chromium dioxide particles. Journal of magnetism and magnetic materials, 260(1-2), 131-140.

Nørgaard Madsen, K. (2004). Angular dependence of the switching field and implications for gyromagnetic remanent magnetization in three-axis alternating-field demagnetization. Geophysical Journal International, 157(3), 1007-1016.

McFadden, P. L. (1981). A theoretical investigation of the effect of individual grain anisotropy in alternating field demagnetization. Geophysical Journal International, 67(1), 35-51.

Milne, G. A., & Dunlop, D. J. (2006). Angular variation of the magnetic properties and reversal mode of aligned single-domain iron nanoparticles. Journal of Geophysical Research: Solid Earth, 111, B12S08, doi:10.1029/2006JB004530.

Schillinger, W. E., Morris, E. R., Coe, R. S., & Finn, D. R. (2016). Development of a 0.5 T magnetic-core alternating-field demagnetizer. Geochemistry, Geophysics, Geosystems, 17(4), 1283-1295.

Stephenson, A., & Collinson, D. W. (1974). Lunar magnetic field palaeointensities determined by an anhysteretic remanent magnetization method. Earth and Planetary Science Letters, 23(2), 220-228.

Stephenson, A. (1983). Changes in direction of the remanence of rocks produced by stationary alternating field demagnetization. Geophysical Journal International, 73(1), 213-239.

Stephenson, A. (1993). Three-axis static alternating field demagnetization of rocks and the identification of natural remanent magnetization, gyroremanent magnetization, and anisotropy. Journal of Geophysical Research: Solid Earth, 98(B1), 373-381.

Stephenson, A., & Shao, J. C. (1994). The angular dependence of the median destructive field of magnetite particles. Geophysical Journal International, 118(1), 181-184.

Stoner, E. C., & Wohlfarth, E. P. (1948). A mechanism of magnetic hysteresis in heterogeneous alloys. Philosophical Transactions of the Royal Society of London. Series A, Mathematical and Physical Sciences, 240(826), 599-642.

Wilson, R. L., & Lomax, R. (1972). Magnetic remanence related to slow rotation of ferromagnetic material in alternating magnetic fields. Geophysical Journal International, 30(3), 295-303.

Yu, Y. (2010). Paleointensity determination using anhysteretic remanence and saturation isothermal remanence. Geochemistry, Geophysics, Geosystems, 11(2).

The IRM Quarterly

The *Institute for Rock Magnetism* is dedicated to providing state-of-the-art facilities and technical expertise free of charge to any interested researcher who applies and is accepted as a Visiting Fellow. Short proposals are accepted semi-annually in spring and fall for work to be done in a 10-day period during the following half year. Shorter, less formal visits are arranged on an individual basis through the Facilities Manager.

The *IRM* staff consists of **Subir Banerjee**, Professor/Founding Director; **Bruce Moskowitz**, Professor/Director; **Joshua Feinberg**, Assistant Professor/Associate Director; **Maxwell Brown, Peat Sølheid** and **Dario Bilardello**, Staff Scientists.

Funding for the *IRM* is provided by the **National Science Foundation**, the **W. M. Keck Foundation**, and the **University of Minnesota**.

UNIVERSITY OF MINNESOTA

The *IRM Quarterly* is published four times a year by the staff of the *IRM*. If you or someone you know would like to be on our mailing list, if you have something you would like to contribute (*e.g.*, titles plus abstracts of papers in press), or if you have any suggestions to improve the newsletter, please notify the editor:

Dario Bilardello
Institute for Rock Magnetism
University of Minnesota
150 John T Tate Hall
116 Church Street SE
Minneapolis, MN 55455-0128
phone: (612) 624-5049
e-mail: dario@umn.edu
www.irm.umn.edu

IRM